

Compact dual MOT apparatus of K and Rb for optical tweezer experiment

Kedi Wei(魏可迪), Yangbo Wei(韦样波), Shangjin Li(李上进), and Bo Yan(颜波)
Citation: Chin. Phys. B, 2026, 35 (**1**): 013701. DOI: 10.1088/1674-1056/ade8e2
http://cpb.iphy.ac.cn; http://iopscience.iop.org/cpb

What follows is a list of articles you may be interested in

Dual-species stimulated deceleration of MgF molecules with Rb atoms

Jin Wei(魏晋), Di Wu(吴迪), Chenyu Zu(祖晨宇), Yong Xia(夏勇), and Jianping Yin(印建平)
Chin. Phys. B, 2025, 34 (**7**): 073701. DOI: 10.1088/1674-1056/adcb1f

A Rb-Cs dual-species magneto-optical trap

Shiyao Shao(邵师尧), Qing Li(李庆), Lihua Zhang(张力华), Bang Liu(刘邦), Zhengyuan Zhang(张正源), Qifeng Wang(王启锋), Jun Zhang(张俊), Yu Ma(马宇), Tianyu Han(韩天宇), Hanchao Chen(陈瀚超), Jiadou Nan(南佳豆), Yiming Yin(殷一鸣), Dongyang Zhu(朱东杨), Yajun Wang(王雅君), Dongsheng Ding(丁冬生), and Baosen Shi(史保森)
Chin. Phys. B, 2025, 34 (**6**): 063702. DOI: 10.1088/1674-1056/adc190

Observation of momentum-induced broadening of width in narrow Feshbach resonances of ultracold ^{133}Cs atoms

Zhennan Liu(刘震南), Hongxing Zhao(赵宏星), Yunfei Wang(王云飞), Yuqing Li(李玉清), Jizhou Wu(武寄洲), Wenliang Liu(刘文良), Peng Li(李鹏), Yongming Fu(付永明), Liantuan Xiao(肖连团), Jie Ma(马杰), and Suotang Jia(贾锁堂)
Chin. Phys. B, 2025, 34 (**2**): 023701. DOI: 10.1088/1674-1056/ad92fc

Compact magneto-optical traps using planar optics

Zhi Tan(谭智), Bo Lu(鹿博), Chengyin Han(韩成银), and Chaohong Lee(李朝红)
Chin. Phys. B, 2024, 33 (**9**): 093701. DOI: 10.1088/1674-1056/ad607a

Atomic transport dynamics in crossed optical dipole trap

Peng Peng(彭鹏), Zhengxi Zhang(张正熙), Yaoyuan Fan(樊耀塬), Guoling Yin(殷国玲), Dekai Mao(毛德凯), Xuzong Chen(陈徐宗), Wei Xiong(熊炜), and Xiaoji Zhou(周小计)
Chin. Phys. B, 2024, 33 (**7**): 073701. DOI: 10.1088/1674-1056/ad401c

---

Compact dual MOT apparatus of K and Rb for optical tweezer experiment

Kedi Wei(魏可迪), Yangbo Wei(韦样波), Shangjin Li(李上进), and Bo Yan(颜波)†

School of Physics, Zhejiang University, Hangzhou 310027, *China*

(Received 4 May 2025; revised manuscript received 21 June 2025; accepted manuscript online 27 June 2025)

The optical tweezer experiment with neutral atoms is widely used for quantum information research. Here, we present a compact dual magneto-optical trap (MOT) setup for a two-species optical tweezer. Rubidium (Rb) atoms are directly captured using a vapor MOT, while potassium (K) atoms are collected via a 2-stage MOT. Both the quadratic and gradient magnetic fields required for the MOT and Zeeman slower are created by permanent magnets. With the help of the Zeeman slower, the K MOT loading efficiency is enhanced by a factor of three. After the MOT stage, we apply D_1 gray molasses to reduce the temperature of the K atoms to 9 μK. Using this apparatus, both Rb and K are loaded into the optical tweezer.

Keywords: atom, molecule, ion cooling methods, atom cooling methods

PACS: 37.10.–x, 37.10.De

DOI: 10.1088/1674-1056/ade8e2 **CSTR:** 32038.14.CPB.ade8e2

1. Introduction

Optical tweezers with neutral atoms are an important platform for quantum computing and quantum simulation, becoming very popular in recent years.[1–8] With the post-select technique,[9–12] one can easily load only one atom into a tweezer with almost unit fidelity. On the other hand, it is relatively easy to capture a single atom from a magneto-optical trap (MOT) using an optical tweezer. This advanced technique has attracted more and more groups to join this field. The number of tweezers in an array reaches several hundreds and even thousands.[13–16] Interesting physics is studied in these optical tweezer platforms.[17–24]

While most tweezer experiments focus on a single species, a few groups have ventured into working with two species, motivated by the goal of creating a single-molecule array.[24–31] For instance, single Na and Cs atoms are captured in an optical tweezer and subsequently formed into single polar molecules through the use of STIRAP.[28,30] Additionally, dual-species Rydberg arrays leverage species-specific addressing frequencies to enable independent control, crosstalk-free measurements, and direct generation of Rydberg-mediated entanglement between atomic species.[32–34] In the case of two-species tweezer experiments, implementing a dual MOT is the initial step. Conventional single-species MOTs cannot meet the experimental requirements for dual-species tweezers. The ultrahigh vacuum environment precludes later introduction of additional atomic species, necessitating integrated multi-species sources during initial system design. This demands a dedicated dual-species MOT apparatus, for which we selected the Rb/K combination. Furthermore, the dual-species MOT serves as a critical platform for heteronuclear quantum systems. Beyond dual-species tweezer experiments, our apparatus facilitates applications in hybrid cold-atom systems, such as quantum memory,[35] and hybrid topological states.[36]

To efficiently load a single atom into an optical tweezer, the beam of the tweezer should be focused to ~ 1 μm.[1,37] Consequently, the optical access of the vacuum chamber must be sufficiently large to accommodate a large numerical aperture, making a glass cell a typical choice. In contrast to traditional Bose–Einstein condensate (BEC) experiments,[38] optical tweezer experiments only require a very dilute MOT for efficient atom loading. During detection, it is crucial to eliminate stray light to distinguish single-atom loading from background scattering. Since fluorescence from background atoms is difficult to block with a spatial filter, it is essential to maintain the background vapor pressure at 10^{-9} Pa. This low pressure is also critical for achieving a long lifetime of atoms in the optical tweezer.

2. Experimental setup

With all these requirements, designing a dual compact MOT apparatus is worthwhile, as illustrated in Fig. 1. The vacuum chamber comprises an uncoated glass cell with internal dimensions of 10 mm × 20 mm × 100 mm, and the thickness of the glass is 2 mm. This design achieves significant compactness through permanent magnets replacing conventional coils. The background vacuum pressure is maintained by a 15-L/s ion pump and reaches 1×10^{-9} Pa. During dual-species operation, background vapor pressures remain at: Rb $< 1 \times 10^{-8}$ Pa, K $< 1 \times 10^{-9}$ Pa. This low-pressure environment ensures negligible crosstalk during atomic loading.

†Corresponding author. E-mail: yanbohang@zju.edu.cn

© 2026 Chinese Physical Society and IOP Publishing Ltd. All rights, including for text and data mining, AI training, and similar technologies, are reserved.

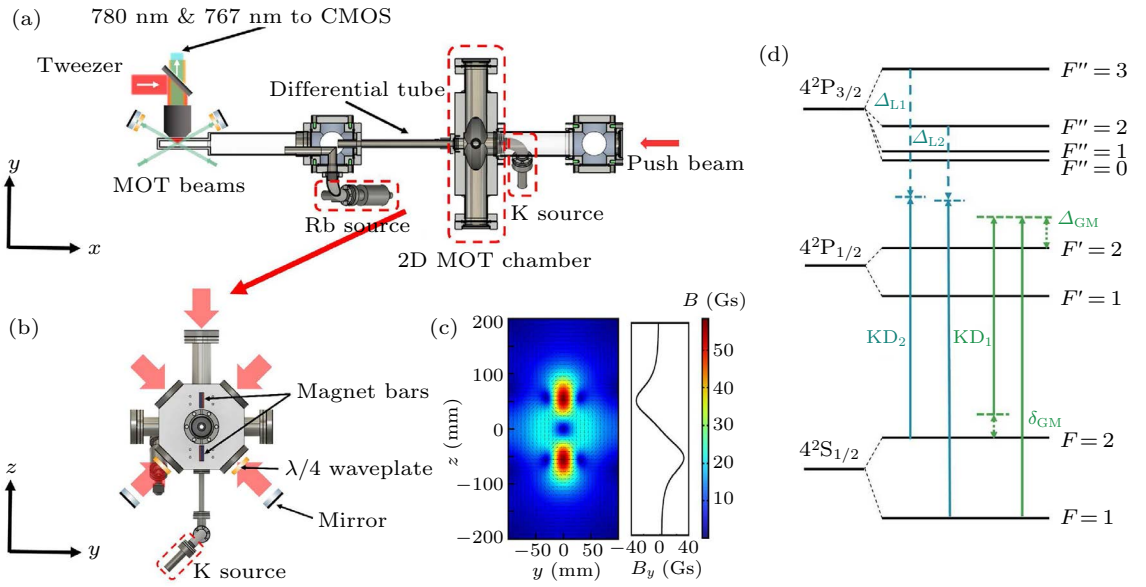


Fig. 1. (a) Top view of the apparatus. The Rb oven is connected to the glass cell, whereas the K oven is directly linked to a two-dimensional (2D) chamber, which in turn is connected to the glass cell via a differential tube. (a) System workflow: K atoms: Captured in 2D MOT chamber → transported via differential pumping tube to the glass cell by push beam → formed into three-dimensional (3D) MOT by MOT beams. Rb atoms: Loaded directly into MOT within the glass cell. Optics: Combined 780 nm (Rb MOT)/767 nm (K MOT)/770 nm (K GM) beams incident; 850-nm optical tweezer beams (red) reflected by a dichroic mirror and focused by an objective lens (NA = 0.25) to capture atoms; Fluorescence signals (Rb 780 nm/K 767 nm) collected by the same objective lens, transmitted through the dichroic filter, and imaged by CMOS. (b) Enlarged view of the 2D MOT chamber. 2D MOT beams: Orthogonally incident at 90° and retro-reflected. Zeeman slower beam: Vertically incident. Magnets: Mounted on the stainless-steel chamber wall via a 3D-printed holder (positionally adjustable). (c) The magnetic field is generated by magnet bars along the *y*- and *z*-axes. The plot on the right depicts the magnetic field amplitude along the slowing beam. (d) The relevant transition for K atoms.

The Rb MOT employs a single-stage design. A stainless steel tube with an inner diameter of 13 mm is connected to the Rb oven and is directly aligned with the MOT region. The background Rb vacuum pressure can be regulated by adjusting the oven temperature. The magnetic field gradient is 11.5 Gs/cm (1 Gs = 10^{-4} T). The MOT beams comprise cooling light and repump light for Rb atoms, as well as cooling light, repump light, and gray molasses (GM) light for K atoms. The cooling and repump lights required for Rb atoms are combined using a polarizing beam splitter (PBS). The lights necessary for K atoms, including cooling, repump, and GM light, are combined via two PBSs; these two beams are then further merged through a dichroic mirror. The radius ($e^{-1/2}$) of the MOT beam is 2.5 mm. The total power of the cooling light for Rb is 8 mW, with a frequency detuning of −11.4 MHz relative to the D_2 line $F = 2 \rightarrow F' = 3$. The repump light has a power of 1.2 mW and is resonant with the $F = 1 \rightarrow F' = 2$ transition of the D_2 line.

3. The K MOT

For K, we use a two-stage setup: K atoms are first collected in a 2D MOT and then pushed to the 3D MOT region. This scheme allows for separate control of the K vacuum pressure, an approach that has been employed with many other atoms, such as Li,[14] Na,[40,41] and Sr.[42] Currently, we are working with ^{39}K and can easily switch to ^{40}K in the future simply by shifting the frequency of the locking point, without any modifications to the remaining optical paths. Our device offers numerous advantages compared to the traditional Zeeman slower;[43–45] these advantages include small size, elimination of the need for complex coil designs for the magnetic field, and prevention of the particle beam directly striking the experimental chamber. The 3D MOT parameters of K are as follows: The total cooling laser has a power of 12.5 mW, with a detuning of −32.7 MHz relative to the D2 line $F = 2 \rightarrow F' = 3$. The repump laser has a power of 7.6 mW, with a frequency detuning of −18.6 MHz relative to the D_2 line of $F = 1 \rightarrow F' = 2$.

The 2D MOT chamber is shown in Fig. 1(b). The four beams, which are inclined at 45 degrees along the *y* and *z* directions, are the 2D MOT beams. Each beam consists of both cooling light and repump light with a power ratio of 1:1, a diameter of 10 mm, and a total power of 75 mW. The frequency of the cooling light is detuned by −33 MHz relative to the D_2 line $F = 2 \rightarrow F' = 3$, while the frequency of the repump light is detuned by −14 MHz relative to the D_2 line $F = 1 \rightarrow F' = 2$. The slowing beam, which is along the *z* direction, has a diameter of 10 mm and a power of 160 mW. The slowing beam also consists of both cooling light and repump light with a cooling-to-repump power ratio of 1:1. The cooling light frequency is detuned by $\Delta_{L1} = -59$ MHz, and the repump light's frequency is detuned by $\Delta_{L2} = -80$ MHz, as indicated in Fig. 1(d). The magnetic field is generated by four magnet arrays. Each array comprises three magnets (N35) with dimensions of 3 mm × 10 mm × 30 mm. These four

magnet sets are positioned at the four corners of a rectangle in the xz plane, with the geometric center of each magnet set aligning with the rectangle's vertices. The rectangle measures 105 mm along the z-axis and 86 mm along the y-axis. The N–S poles of the two magnet sets along the z-axis are oriented in opposite directions, whereas those along the y-axis are aligned in the same direction. The permanent magnet array is secured within a high-precision 3D-printed fixture mounted on the stainless-steel octagonal chamber using threaded mounting with adjustable screws. This design supports two methods for magnetic field adjustment: (i) replacing the fixture housing or fine-tuning the position of individual magnet sub-assemblies; (ii) replacing magnet grades (*e.g.*, N35 → N52) or varying the number of magnets. The magnetic field is shown in Fig. 1(c). Near the center, the magnetic field gradient is 13 Gs/cm. Ultimately, these conditions result in a 2D capture velocity of 44 m/s. There is a long tail of approximately 200 mm and a maximum magnetic field of 58 Gs. The Zeeman slowing primarily operates from $z = -200$ mm to $z = -20$ mm.

Figure 2 presents the experimental results of the K MOT. Figure 2(a) illustrates the K MOT filling curves with and without the slowing beam. With the Zeeman slower in operation, the MOT number increases by approximately a factor of 3. Figure 2(b) depicts the MOT number $N_{\text{K-MOT}}$ after a 500-ms filling time as a function of the detuning of the slowing beam (labeled as Δ_{L1}). The maximum MOT number is observed at $\Delta_{\text{L1}} = -59$ MHz and decreases rapidly when $\Delta_{\text{L1}} > -50$ MHz.

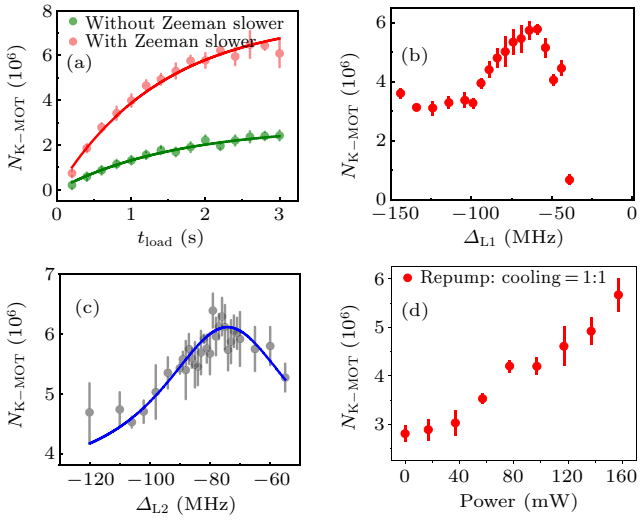


Fig. 2. The K MOT data. Panel (a) shows the loading curves of the K MOT with and without the Zeeman slower. The operating conditions of the Zeeman slower are: $\Delta_{\text{L1}} = -59$ MHz, $\Delta_{\text{L2}} = -80$ MHz, and the total optical intensity is 160 mW. Horizontal axis: 3D MOT loading time (in unit s); Vertical axis: Atom number calibrated by absorption imaging. Panels (b), (c), and (d) respectively show the dependence of the MOT number on the detuning of the slowing light, the detuning of the repump light, and the power of the slowing light in the Zeeman slower. For each graph, while scanning the specified parameter, the remaining parameters were set to their optimized values. Panels (b), (c), and (d) reveal the optimal deceleration parameters: $\Delta_{\text{L1}} = -59$ MHz, $\Delta_{\text{L2}} = -80$ MHz. Regarding the Zeeman slower beam intensity, higher power is preferable within the tested range (up to 160 mW).

Figure 2(c) illustrates the dependence of $N_{\text{K-MOT}}$ on the slowing repump detuning (labeled as Δ_{L2}). The optimal loading is achieved at $\Delta_{\text{L2}} = -80$ MHz. Figure 2(d) depicts the relationship between $N_{\text{K-MOT}}$ and the slowing power. Under the experimental conditions, higher power results in better MOT loading.

To understand the behavior of the K MOT, we have performed numerical simulations. The velocity distribution of undecelerated atoms follows the velocity distribution of atoms ejected from a nozzle, as given by[46]

$$P_{\text{exit}}(v)\,\mathrm{d}v = 2\left(\frac{m}{2k_{\text{B}}T}\right)^2 v^3 \exp\left(\frac{-mv^2}{2k_{\text{B}}T}\right)\mathrm{d}v. \tag{1}$$

The program employs a numerical integration method, specifically the fourth-order Runge–Kutta method, to solve the equations of motion for atoms interacting with laser fields and magnetic gradients. The primary objective is to determine the final velocity distribution of atoms after they traverse the Zeeman slower and enter the 2D MOT region. The numerical simulation calculations are based on the following simplifications.

(i) We simplify the model to a two-level system subject to classical radiation pressure, given by

$$F = \frac{\Gamma\hbar k}{2}\frac{I/I_{\text{sat}}}{1+4(\Delta/\Gamma)^2+I/I_{\text{sat}}}, \tag{2}$$

where I denotes the intensity of the decelerating light beam, and $\Delta = \Delta_{\text{L}} + \Delta_{\text{Doppler}} + \Delta_{\text{Zeeman}}$.

(ii) Only the one-dimensional case is considered.

Formula (2) employs a simplified two-level model and does not include the effects of hyperfine structure (other transitions are significantly detuned due to the Zeeman shift, contributing minimally to the scattering force). This simplification is also used in similar studies, such as Barker *et al.*[44] However, it is important to note: For potassium atoms (^{39}K), the hyperfine splitting on the D_2 line is relatively small (on the order of Γ). Furthermore, in our experimental configuration, the Zeeman slower's magnetic field increases gradually from a low value. This initial phase during deceleration could potentially lead to population leakage into other hyperfine levels.

Figure 3(a) illustrates the evolutions of atoms with different initial velocities when using a laser intensity of $15I_{\text{s}}$ and a slowing detuning of $\Delta_{\text{L1}} = -86$ MHz. The region to the right of the black dashed line in the figure indicates where 2D cooling begins to take effect, and this dashed line represents the turning position of the magnetic field. Notably, some atoms with lower initial velocities have their speeds reduced to zero midway, ultimately failing to reach the 2D cooling region. Conversely, atoms with excessively high initial velocities remain unaffected by the Zeeman slower. In Fig. 3(b), it is evident that the gain increases with rising slowing light intensity before it reaches 50 times the saturation intensity. This trend was experimentally confirmed, as shown in Fig. 2(d).

Furthermore, figure 3(b) reveals that excessive light intensity leads to a decrease in gain as it increases. This decrease stems from the fact that, as the deceleration light intensifies, low-speed atoms are decelerated to a standstill, preventing them from reaching the 2D area and subsequently reducing the gain. Due to experimental constraints, we could not achieve sufficiently high laser power to observe this phenomenon. The inset illustrates that, theoretically, the maximum gain is achieved at a detuning of $\Delta_{L1} = -86$ MHz for the Zeeman cooling light when using a light intensity of $15I_{S0}$ (as utilized in our experiment). Nevertheless, our experimental results deviate, with the maximum gain observed at $\Delta_{L1} = -59$ MHz, and the experimental gain effect proving less pronounced than anticipated. We hypothesize that this discrepancy may arise from our simulation model, which considers only one dimension.

Figure 3(c) shows the velocity distribution before and after slowing. Through the application of the Zeeman slower, we observe an increase in the atomic distribution within the lower velocity region. In Fig. 3(d), we compute the final velocities of atoms post-deceleration, correlating them with their different initial velocities. These figures illustrate that our Zeeman slower effectively decelerates atoms possessing initial velocities of 100 m/s or less, concentrating their resultant velocities in the vicinity of 35 m/s. Nonetheless, a segment of the low-velocity atoms (19 m/s and below) is decelerated to zero.

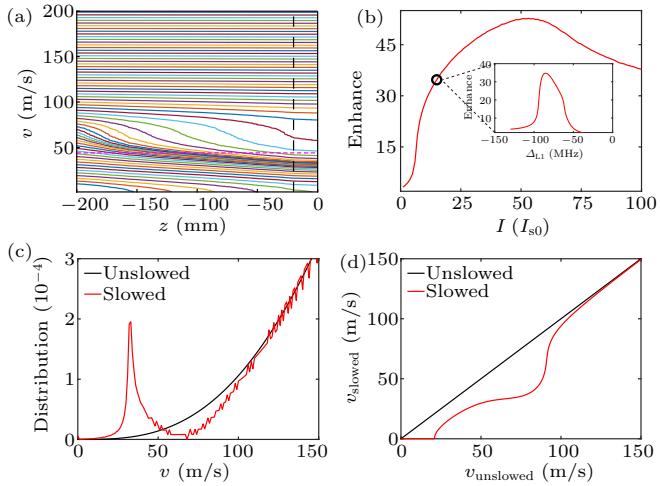


Fig. 3. The simulation results of the K Zeeman slower. Panel (a) shows the trajectories of atoms with different initial velocities in the Zeeman slower, with a laser intensity of $15I_s$ and a slowing detuning of $\Delta_{L1} = -86$ MHz; the black dashed line represents the position where the deceleration effect ends. Panel (b) shows the dependence of enhancement on the slowing laser power, with a slowing detuning of $\Delta_{L1} = -86$ MHz; the inset shows the dependence of the detuning Δ_{L1}, with a laser intensity of $15I_s$. Panel (c) presents the velocity distribution before and after the Zeeman slower, the expression for which is given by formula (1). Panel (d) displays the corresponding final velocities of atoms with different initial velocities after deceleration. The parameters used in the simulations for panels (c) and (d) are the same as those for panel (a).

In conclusion, in our simulation calculations, we predicted that the gain would increase with the increase of light intensity when it is less than 50 times the saturation intensity, and we observed this trend in our experiments. Additionally, at $15I_S$ light intensity, simulations predict maximum gain at $\Delta_{L1} = -86$ MHz, exceeding 30-fold. Experimentally, we achieved the maximum gain at -59 MHz, with a gain of 3 times. This discrepancy is due to the fact that our simulation model only simply considers a two-level system and a one-dimensional situation. The discrepancy also stems from: (i) The one-dimensional model neglecting atomic beam divergence,[44] reducing gain by $\sim 60\%$. Although the simulation results did not perfectly match the experimental results, they provided us with directions for optimizing the experiment, such as using higher light intensities to achieve greater gains and collimating the emitted atoms to better utilize the deceleration magnetic field.

4. Gray molasses of K

After loading for 500 ms, the 3D MOT of K can capture about 1×10^6 atoms. Subsequently, we perform polarization gradient cooling (PGC). During this process, the gradient magnetic field is ramped down from 11.5 Gs/cm to zero within 4 ms, the cooling light detuning is changed from -32.7 MHz to -7 MHz, and the power is reduced from 12.5 mW to 240 μW, ultimately cooling the atoms to 50(5) μK. However, this temperature is still too high for subsequent tweezer loading. To further cool the K atoms, we employ Λ-enhanced gray molasses (GM) on the D_1 transition. The core mechanism of D1 gray molasses cooling lies in the synergistic action of polarization gradient cooling (Sisyphus cooling) and velocity-selective coherent population trapping (VSCPT). (i) In Sisyphus cooling, atoms traverse spatially varying polarization light fields, experiencing periodic light-shift potentials. Net cooling is achieved through the conversion of kinetic energy to potential energy and subsequent spontaneous emission. (ii) The VSCPT mechanism prepares atoms in long-lived dark states under the two-photon Raman resonance condition ($\delta = 0$ MHz). The escape rate from these dark states scales quadratically with atomic velocity ($\Gamma_{esc} \propto v^2$), thereby selectively trapping slower atoms. The key rationale for selecting the D_1 line (over the D_2 line) is its excited state ($4P_{1/2}$), which possesses more degenerate hyperfine levels. This facilitates the formation of efficient dark states, avoiding the heating effects caused by level mixing inherent to the D_2 line ($4P_{3/2}$). The GM beams, along with the 3D MOT beams, are combined and sent through the same optical path into the glass cell with a total power of 4 mW and a diameter of 5 mm, where the ratio of cooling to repump light intensity is 3:1. Figure 4(a) illustrates the sensitivity of GM cooling efficiency to two-photon detuning; the optimal cooling effect is achieved at

0 MHz, and there is no cooling effect beyond ±0.2 MHz. This is a characteristic of the Sisyphus cooling mechanism with dark states.[47] Figure 4(b) demonstrates that the cooling effect of GM is insensitive to single-photon detuning in the far-detuned region, showing cooling effects across a wide range from +20 MHz to +60 MHz. Approaching resonance leads to heating,[47,48] which is also illustrated in Fig. 4(b), where the final temperature of the atomic ensemble near resonance is even higher than that before cooling. With the help of GM, the temperature of the K atoms is further reduced to approximately 9 μK under optimized conditions, which is sufficient for our subsequent optical tweezer experiments.

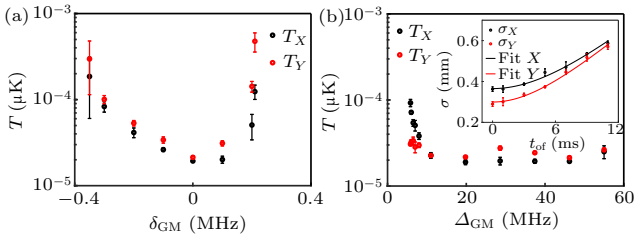


Fig. 4. Panels (a) and (b) respectively show the relationships between the temperature of gray Molasses and two-photon detuning (δ_{GM}) and one-photon detuning (Δ_{GM}). The inset demonstrates the measurement of the atomic temperature utilizing the time-of-flight method with $\delta_{GM} = 0$ MHz and $\Delta_{GM} = +47$ MHz. Under these conditions, the temperature of the K atoms is reduced to approximately 9 μK. The optimal cooling effect observed at zero two-photon detuning ($\delta_{GM} = 0$ MHz) in panel (a) provides direct evidence for dark state formation via the VSCPT mechanism. The plateau in temperature observed for single-photon detunings $\Delta_{GM} > +20$ MHz in panel (b) reflects the stability of Sisyphus cooling in the far-detuned regime.

5. Dual MOT and optical twezzer

Figures 5(a) and 5(b) show the MOT loading of dual-species. The MOT loading of single-species and dual-species is consistent with each other within the error bars, which means there is no crosstalk between them. After loading the MOT for 500 ms, we apply PGC for Rb and D_1 gray molasses to K, reducing the temperature to 10 μK for Rb and 9 μK for K. Then we load them into an optical tweezer (2.1 μm). The photon count distribution can be modeled as a Gaussian distribution[1,49]

$$P(N = x|i) = \frac{1}{d_i\sqrt{2\pi}} \exp\left(-\frac{(x-u_i)^2}{2d_i^2}\right), \tag{3}$$

where N represents the number of photons collected. $i = 0$ for no atom loading and $i = 1$ for an atom being loaded. d_i and u_i are the parameters that we need to fit. The overall photon count distribution can be expressed as

$$P(N = x) = BP(N = x|1) + (1 - B)P(N = x|0), \tag{4}$$

in which B denotes the probability of loading an atom.

Figures 5(c) and 5(d) show that the single Rb filling ratio in an optical tweezer is about 0.52 (3), and the K filling ratio in an optical tweezer is about 0.49 (4). This is a good starting point for further optical tweezer experiments.

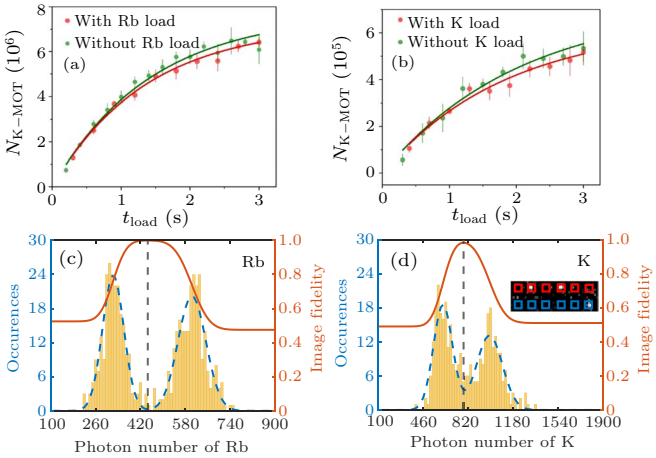


Fig. 5. (a) The K MOT loading curves with and without the Rb MOT. (b) The Rb MOT loading curves with and without the K MOT. Current imaging employs temporal separation: both MOT beams are active during the loading phase, while only single-species imaging light (Rb or K) is activated during the detection phase. Panels (a) and (b) demonstrate that the atom numbers show no significant difference (within experimental uncertainty) when the Rb/K dual MOT are loaded simultaneously. This indicates that the MOTs for the two species operate without mutual interference. Panels (c) and (d) show the optical tweezer signals for K and Rb, respectively. The orange curve represents the fitting of a bimodal Gaussian distribution. Integration time for photon counts (horizontal axis) in panels (c) and (d): 100 ms. Inset in panel (d): Single-shot imaging showing tweezer 2 and 4 loaded with Rb atom (red boxes) and tweezer 6 loaded with K atom (blue box).

6. Conclusion

In conclusion, we have presented a compact dual-species MOT system optimized for optical tweezer experiments with both potassium and rubidium atoms. Through innovative design, we have achieved efficient trapping and cooling of both species. The implementation of a Zeeman slower has significantly increased the number of trapped potassium atoms. The D_1 gray molasses efficiently reduces the temperature of K atoms, resulting in successful loading into optical tweezers for both Rb and K atoms.To further reduce the K atom temperature (currently 9 μK), future work will focus on: (i) optical path optimization: Refining the six-beam gray molasses (GM) optical alignment; (ii) magnetic field stabilization: Implementing active feedback or magnetic shielding (motivated by GM sensitivity to two-photon detuning and differential Zeeman shifts between $F = 1 \to F' = 2$ and $F = 2 \to F' = 2$ transitions); (iii) temporal sequence refinement: Adopting a staged cooling protocol (high-intensity rapid cooling followed by low-intensity deep cooling);[47] (iv) parameter space exploration: Systematic optimization of single-/two-photon detuning and intensity ratio. Based on the demonstrated coexistence of dual MOT and the capability for simultaneous dual-species optical tweezer capture, this system meets the fundamental prerequisites for molecular synthesis experiments. The current system achieves compactness through a permanent-magnet Zeeman slower (replacing electromagnetic coils) and a miniaturized glass cell (10 mm×20 mm×100 mm, Fig. 1). Future implementations may integrate metasurface

chip technology[50] for further miniaturization, while dual-tweezer integration schemes[51] could expand multifunctional applications.

Acknowledgements

Project supported by the National Key Research and Development Program of China (Grant Nos. 2023YFA1406703 and 2022YFA1404203), the National Natural Science Foundation of China (Grant Nos. 12425408, U21A20437 and 12074337), the Natural Science Foundation of Zhejiang Province, China (Grant No. LR21A040002), and the Fundamental Research Funds for the Central Universities (Grant No. 226-2023-00131).

References

[1] Schlosser N, Reymond G, Protsenko I and Grangier P 2001 *Nature* **411** 1024
[2] Zhang X L, Isenhower L, Gill A T, Walker T G and Saffman M 2010 *Phys. Rev. A* **82** 030306
[3] Wilk T, Gaëtan A, Evellin C, Wolters J, Miroshnychenko Y, Grangier P and Browaeys A 2010 *Phys. Rev. Lett.* **104** 010502
[4] Kaufman A M, Lester B J and Regal C A 2012 *Phys. Rev. X* **2** 041014
[5] Lester B J, Luick N, Kaufman A M, Reynolds C M and Regal C A 2015 *Phys. Rev. Lett.* **115** 073003
[6] Kaufman A M and Ni K K 2021 *Nat. Phys.* **17** 1324
[7] Liu J, Wu X, Feng Y, Zheng M and Li Z 2023 *Chin. Phys. B* **32** 108704
[8] Wen K, Chen H, Yan X, Ren Z, He C, Hajiyev E, Fung Wong P T and Jo G B 2024 *Chin. Phys. B* **33** 120703
[9] Weiss D S, Vala J, Thapliyal A V, Myrgren S, Vazirani U and Whaley K B 2004 *Phys. Rev. A* **70** 040302
[10] Barredo D, de Leseleuc S, Lienhard V, Lahaye T and Browaeys A 2016 *Science* **354** 1021
[11] Endres M, Bernien H, Keesling A, Levine H, Anschuetz E R, Krajenbrink A, Senko C, Vuletic V, Greiner M and Lukin M D 2016 *Science* **354** 1024
[12] Sheng C, Hou J, He X, Xu P, Wang K, Zhuang J, Li X, Liu M, Wang J and Zhan M 2021 *Phys. Rev. Res.* **3** 023008
[13] Tian W, Wee W J, Qu A, Lim B J M, Datla P R, Koh V P W and Loh H 2023 *Phys. Rev. Appl.* **19** 034048
[14] Tao R, Ammenwerth M, Gyger F, Bloch I and Zeiher J 2023 arXiv: 2309. 04717
[15] Huft P, Song Y, Graham T M, Jooya K, Deshpande S, Fang C, Kats M and Saffman M 2022 *Phys. Rev. A* **105** 063111
[16] Lorenz N, Festa L, Steinert L M and Gross C 2021 *SciPost Phys.* **10** 052
[17] Bernien H, Schwartz S, Keesling A, Levine H, Omran A, Pichler H, Choi S, Zibrov A S, Endres M, Greiner M, Vuletic V and Lukin M D 2017 *Nature* **551** 579
[18] Ebadi S, Wang T T, Levine H, Keesling A, Semeghini G, Omran A, Bluvstein D, Samajdar R, Pichler H, Ho W W, Choi S, Sachdev S, Greiner M, Vuletic V and Lukin M D 2021 *Nature* **595** 227
[19] Scholl P, Schuler M, Williams H J, Eberharter A A, Barredo D, Schymik K N, Lienhard V, Henry L P, Lang T C, Lahaye T, Laeuchli A M and Browaeys A 2021 *Nature* **595** 233
[20] Bluvstein D, Evered S J, Geim A A, Li S H, Zhou H, Manovitz T, Ebadi S, Cain M, Kalinowski M, Hangleiter D, Ataides J P B, Maskara N, Cong I, Gao X, Sales Rodriguez P, Karolyshyn T, Semeghini G, Gullans M J, Greiner M, Vuletic V and Lukin M D 2024 *Nature* **626** 58
[21] Norcia M A, Young A W, Eckner W J, Oelker E, Ye J and Kaufman A M 2019 *Science* **366** 93
[22] Young A W, Eckner W J, Milner W R, Kedar D, Norcia M A, Oelker E, Schine N, Ye J and Kaufman A M 2020 *Nature* **588** 408
[23] Jenkins A, Lis J W, Senoo A, McGrew W F and Kaufman A M 2022 *Phys. Rev. X* **12** 021027
[24] Ni K K, Ospelkaus S, de Miranda M H G, Pe'er A, Neyenhuis B, Zirbel J J, Kotochigova S, Julienne P S, Jin D S and Ye J 2008 *Science* **322** 231
[25] Takekoshi T, Reichsöllner L, Schindewolf A, Hutson J M, Le Sueur C R, Dulieu O, Ferlaino F, Grimm R and Nägerl H C 2014 *Phys. Rev. Lett.* **113** 205301
[26] Park J W, Will S A and Zwierlein M W 2015 *Phys. Rev. Lett.* **114** 205302
[27] Guo M, Zhu B, Lu B, Ye X, Wang F, Vexiau R, Bouloufa-Maafa N, Quéméner G, Dulieu O and Wang D 2016 *Phys. Rev. Lett.* **116** 205303
[28] Liu L R, Hood J D, Yu Y, Zhang J T, Hutzler N R, Rosenband T and Ni K K 2018 *Science* **360** 900
[29] Zhang J T, Yu Y, Cairncross W B, Wang K, Picard L R B, Hood J D, Lin Y W, Hutson J M and Ni K K 2020 *Phys. Rev. Lett.* **124** 253401
[30] Cairncross W B, Zhang J T, Picard L R B, Yu Y, Wang K and Ni K K 2021 *Phys. Rev. Lett.* **126** 123402
[31] Ruttley D K, Guttridge A, Spence S, Bird R C, Le Sueur C R, Hutson J M and Cornish S L 2023 *Phys. Rev. Lett.* **130** 223401
[32] Anand S, Bradley C E, White R, Ramesh V, Singh K and Bernien H 2024 *Nat. Phys.* **20** 1744
[33] Zeng Y, Xu P, He X, Liu Y, Liu M, Wang J, Papoular D J, Shlyapnikov G V and Zhan M 2017 *Phys. Rev. Lett.* **119** 160502
[34] Sheng C, Hou J, He X, Wang K, Guo R, Zhuang J, Mamat B, Xu P, Liu M, Wang J and Zhan M 2022 *Phys. Rev. Lett.* **128** 083202
[35] Ding D S, Zhang W, Zhou Z Y, Shi S, Xiang G Y, Wang X S, Jiang Y K, Shi B S and Guo G C 2015 *Phys. Rev. Lett.* **114** 050502
[36] Li T, Liu M, Qin J, Ren J, Hou J, Liu Y, Yang X, Chu H, Lai Y, Wang S, Jiang J H, Chan C T and Zhu S 2025 *Nat. Sci. Rev.* **12** nwaf107
[37] Schlosser N, Reymond G and Grangier P 2002 *Phys. Rev. Lett.* **89** 023005
[38] Li Y, Liu Z, Wang Y, Wu J, Liu W, Fu Y, Li P, Ma J, Xiao L and Jia S 2023 *Chin. Phys. B* **32** 103701
[39] Tiecke T G, Gensemer S D, Ludewig A and Walraven J T M 2009 *Phys. Rev. A* **80** 013409
[40] Lamporesi G, Donadello S, Serafini S and Ferrari G 2013 *Rev. Sci. Instrum.* **84** 063102
[41] Li Z L, Shi Z L and Wang P J 2020 *Acta Phys. Sin.* **69** 126701 (in Chinese)
[42] Nosske I, Couturier L, Hu F, Tan C, Qiao C, Blume J, Jiang Y H, Chen P and Weidemüller M 2017 *Phys. Rev. A* **96** 053415
[43] Lasner Z, Mitra D, Hiradfar M, Augenbraun B, Cheuk L, Lee E, Prabhu S and Doyle J 2021 *Phys. Rev. A* **104** 063305
[44] Barker D, Norrgard E, Klimov N, Fedchak J, Scherschligt J and Eckel S 2019 *Phys. Rev. Appl.* **11** 064023
[45] Yang W, Sun D L, Zhou L, Wang J and Zhan M S 2014 *Acta Phys. Sin.* **63** 153701 (in Chinese)
[46] Giordmaine J A and Wang T C 1960 *J. Appl. Phys.* **31** 463
[47] Salomon G, Fouché L, Wang P, Aspect A, Bouyer P and Bourdel T 2014 *Europhys. Lett.* **104** 63002
[48] Grier A T, Ferrier-Barbut I, Rem B S, Delehaye M, Khaykovich L, Chevy F and Salomon C 2013 *Phys. Rev. A* **87** 063411
[49] Manetsch H J, Nomura G, Bataille E, Leung K H, Lv X and Endres M 2024 *A tweezer array with* 6100 *highly coherent atomic qubits*
[50] Jin M, Zhang X, Liu X, Liang C, Liu J, Hu Z, Li K, Wang G, Yang J, Zhu L and Li G 2023 *Nano Lett.* **23** 4008
[51] Li T, Xu X, Fu B, Wang S, Li B, Wang Z and Zhu S 2021 *Photon. Res.* **9** 1062